Mechanistic basis for motor-driven membrane constriction by dynamin

Oleg Ganichkin[1], Renee Vancraenenbroeck[2], Gabriel Rosenblum[3], Hagen Hofmann[3], Alexander S. Mikhailov[4,5], Oliver Daumke[1,6,7], and Jeffrey K. Noel[1,4,7]

[1]Crystallography, Max Delbrück Center for Molecular Medicine, Berlin, Germany
[2]Department of Structural and Molecular Biology, University College London, London, United Kingdom
[3]Department of Structural Biology, Weizmann Institute of Science, Rehovot, Israel
[4]Department of Physical Chemistry, Fritz Haber Institute of the Max Planck Society, Berlin, Germany
[5]Computational Molecular Biophysics, WPI Nano Life Science Institute, Kanazawa University, Kanazawa, Japan
[6]Institute for Chemistry and Biochemistry, Free University of Berlin, Berlin, Germany
[7]To whom correspondence should be addressed: jeffrey.noel@mdc-berlin.de, oliver.daumke@mdc-berlin.de

Abstract

The mechano-chemical GTPase dynamin assembles on membrane necks of clathrin-coated vesicles into helical oligomers that constrict and eventually cleave the necks in a GTP-dependent way. It remains not clear whether dynamin achieves this via molecular motor activity and, if so, by what mechanism. Here, we used ensemble kinetics, single-molecule FRET and molecular dynamics simulations to characterize dynamin's GTPase cycle and determine the powerstroke strength. The results were incorporated into a coarse-grained structural model of dynamin filaments on realistic membrane templates. Working asynchronously, dynamin's motor modules were found to collectively constrict a membrane tube. Force is generated by motor dimers linking adjacent helical turns and constriction is accelerated by their strain-dependent dissociation. Consistent with experiments, less than a second is needed to constrict a membrane tube to the hemi-fission radius. Thus, a membrane remodeling mechanism relying on cooperation of molecular ratchet motors driven by GTP hydrolysis has been revealed.

Introduction

Dynamin is a mechano-chemical GTPase that plays a central role in clathrin-mediated endocytosis (CME) [1–4]. It is recruited to the endocytic membrane neck where it forms oligomeric helical filaments that constrict and cleave the neck. Dynamin-mediated membrane scission is crucial for cellular nutrient uptake and for regeneration of synaptic vesicles; mutations in this protein are associated with severe human disease [5]. Because of its importance, dynamin has been extensively studied, but understanding of its principal GTP-dependent function could not yet be reached [6]. Two alternative mechanisms are currently under discussion [6], i.e. (i) a

more passive one, in which membrane constriction occurs by equilibrium assembly of dynamin filaments and GTP hydrolysis is only required for final cleavage [7–9], and (ii) a mechanism with the constriction resulting from mechanical work by molecular motors powered by GTP hydrolysis [3, 6]. Here, we provide clear experimental and computational evidence in favor of the molecular motor mechanism, with strong parallels to the operation of muscle myosin.

Dynamin consists of five domains, four of which have been structurally characterized [10–12]: a GTPase (G) domain, a bundle signaling element (BSE), a stalk, and a pleckstrin homology (PH) domain (Figure 1A). The C-terminal proline-rich domain is predicted to be mostly disordered and contains SH3 domain binding motifs involved in the recruitment to membrane necks during CME [13]. A combination of crystallographic and cryogenic electron microscopic (cryo-EM) studies has elucidated the overall architecture of dynamin in solution and bound to tubular membranes [10–12, 14, 15]. The stalks dimerize in a criss-cross fashion to form a dimeric building block that further assembles via two additional stalk interfaces into a tetramer (Figure 1B). Binding preferentially to phosphatidylinositol 4,5-bisphosphate (PIP_2)-containing membranes via the PH domain, dynamin forms right-handed helical filaments with apolar symmetry using the same stalk interfaces that are used for assembly in the tetramer (Figure 1C). Distal from the membrane, the G domains are connected to the stalk through the BSE via two hinges. Hinge 1 connects the BSE with the stalk and hinge 2 links the G domain to the BSE.

Membrane constriction and fission can be reconstituted using only dynamin, GTP, and a suitable membrane template [16, 17]. Using such a minimal set-up, it was found that the dynamin helix generates torque [16, 18], suggesting an intrinsic motor activity [2, 6]. When the helical structure of the filament was elucidated [10,12,15], the proximity of G domains explained the membrane-stimulated GTPase activity of dynamin [14], and suggested that their dimerization should play an important role in the motor mechanism. Additionally, the conformation of the G domain relative to the BSE was found to be sensitive to the nucleotide state [15, 19]. In the presence of the non-hydrolyzable GTP analog β,γ-methyleneguanosine 5′-triphosphate (GMPPCP), the G domain/BSE fusion (henceforth referred to as the *motor module*, MM, see Figure 1) crystallized as a dimer with the BSE in an open conformation relative to the G domain [15]. Alternatively, the nucleotide-free MM or the MM bound to GDP·AlF_4^- (a mimic of the transition state of GTP hydrolysis) or GDP crystallized into a closed conformation with the BSE tightly contacting the G domain [10, 11, 14, 20] (Figure 1D). These structural studies led to the hypothesis that a power stroke is responsible for the motor function of dynamin. However, because even slight conformational preferences may result in different crystal states, it remains not certain whether the stroke is powerful enough to generate the required force for membrane constriction.

Theoretical studies of dynamin were focused on the elastic properties of the dynamin filament [22–24] or on how membrane tube stability is affected by helical confinement [25, 26]. Recently, it was shown that dynamin can adapt to varying membrane tube radii via a flexible tetrameric stalk interface [10, 24]. A detailed coarse-grained, polymer-like model of an elastic dynamin filament on a deformable membrane tube was constructed to describe their joint evolution in absence of GTP, and it was demonstrated that, by passive constriction, the hemi-fission radius cannot be reached [24]. So far, the non-equilibrium motor activity based on GTP hydrolysis has been treated only in an abstract phenomenological way [27].

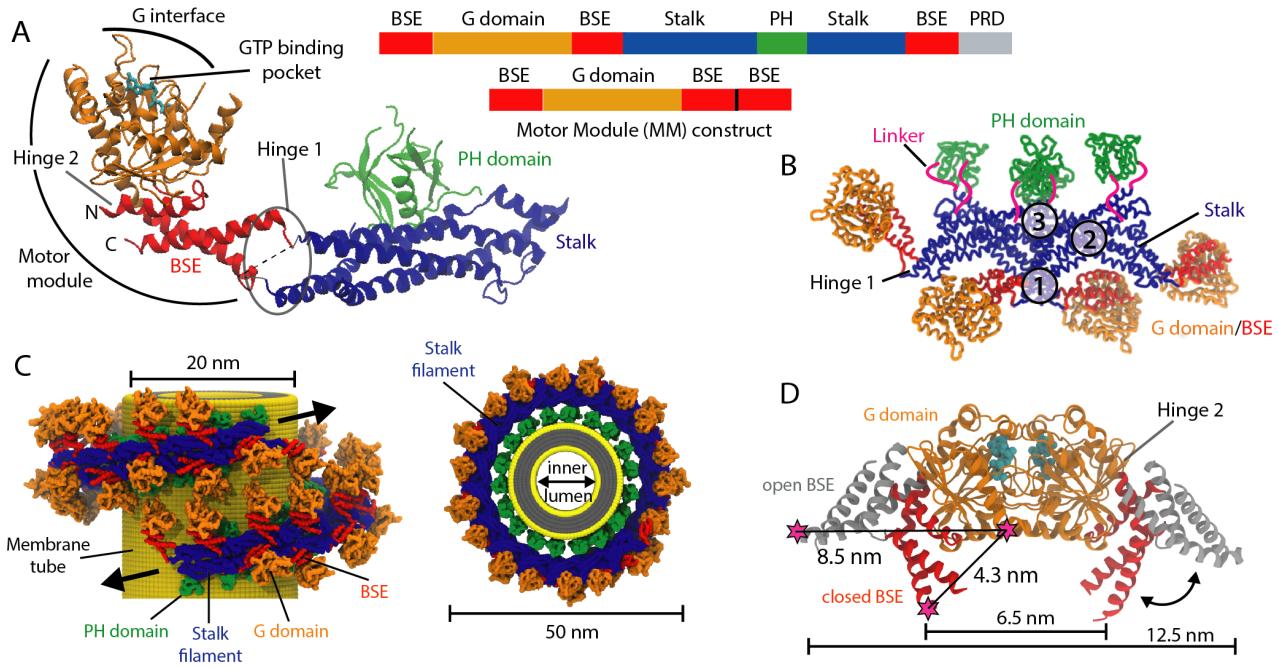

Figure 1: Structural insights into dynamin. A) Dynamin monomer with its four structurally characterized domains (PDB 3SNH [10]). The motor module (MM) contains the G domain and the BSE. A continuous MM construct was created by fusing the third helix of the BSE onto the N-terminal portion of the dynamin sequence. B) Architecture of the dynamin stalk tetramer. The repeating dimeric unit in the filament is stabilized by interface 2 and interfaces 1/3 constitute the oligomerization interface between dimers. The PH domain locations are placed approximately as they appear in cryo-EM reconstructions, connected by flexible linkers. C) Model of a dynamin filament wrapped around a membrane tube based on the non-constricted state cryo-EM structure [10, 21]. MM in orange/red, stalk in blue, PH domain in green, and the membrane bilayer in yellow/gray. D) The MM dimerizes via the G interface. Crystal structures of a similar MM construct reveal a nucleotide-dependent conformational change of the BSE relative to the G domain. In red and orange, the GDP-bound [20] structure is in a closed state where the BSE is closely packed against the G domain. In grey, the BSE of the GMPPCP-bound structure [15] takes an open state where the BSE is extended away from the G domain. The G domain is mostly unchanged between structures (not shown). Magenta stars indicate the locations of cysteine mutations introduced in order to link FRET probes. The crystal structures predict that the conformational change will lead to a 40 Å shift in probe separation.

To validate the molecular motor mechanism of membrane remodeling by dynamin, we characterize the conformational state of the MM by single molecule FRET (smFRET) and show that the MM exhibits strong nucleotide-dependent shifts. Using smFRET populations as a guide for computational molecular dynamics (MD), we determined the forces generated by a single MM dimer. With this data, motor activity was then incorporated into the existing polymer-like model [24]. Through simulations, we found that collective operation of many MM dimers can constrict the membrane down to the hemi-fission radius at which spontaneous scission can take place.

Results

Nucleotide kinetics of the motor module

We aimed at providing a detailed model that explains whether and how the enzymatic activity of dynamin generates the necessary force for membrane constriction. To this end, we began by characterizing the kinetic parameters of dynamin's GTPase cycle along with its impact on the structural state of dynamin by studying a MM construct containing only the G domain and BSE (Figure 1A) [14,28]. Nucleotide association and dissociation rates for the monomeric MM are fundamental to the GTPase cycle and were analyzed by using fluorescently-labeled mant-nucleotides and stopped-flow kinetics (Figure 2A-C). For the non-hydrolyzable GTP analogue, guanosine-5'-(γ-thio)-triphosphate (GTPγS), we obtained an association (on) rate of 1.2 $s^{-1}\mu M^{-1}$ and a dissociation (off) rate of 27 s^{-1}, yielding a K_d of 23 μM (Table 1). Both on and off rates for GDP were about 5-fold faster, resulting in a similar K_d. Interestingly, the binding kinetics for mant-GTP required a fit with two exponentials, with one concentration-dependent rate of 5 $s^{-1}\mu M^{-1}$ and a second concentration-independent rate of 20 s^{-1}, which indicates the formation of a long-lived encounter complex (Figure S1).

The nucleotide binding kinetics indicate that the MM is dominantly GTP-bound in the cell. The affinities for GTP and GDP are similar ($\sim$ 20 μM) (Table 1) and, thus, at physiological nucleotide concentrations, where GTP is roughly 300 μM and GDP is 30 μM [29], ≈90% of monomeric MM is GTP bound. Previous reports of the K_d for mant-GTP in full length bovine dynamin I (2.5 μM [30]) and rat dynamin II (0.5 μM [31]) would suggest even higher GTP occupancy, however, these values may include contributions from nucleotide-induced assembly.

The slow basal GTPase rate k_{hyd}^{basal} of full-length dynamin is 0.1-1 min^{-1} [31,32] but increases 200-fold in the presence of lipid template [10]. This is in line with an assembly-driven activation mechanism that involves the dimerization of MMs. Consistently, we observed a very low basal GTPase rate and a linear increase in the specific hydrolysis rate k_{hyd}^{spec} in the MM concentration range 1 μM< [MM] < 50 μM (Figure 2D,E and SI Section S1.1). These results confirm that the hydrolysis rate is controlled by the population of GTP-bound MM dimers. Since linearity is expected to break down when [MM] $\sim K_d^{dimer}$, the GTPase assay indicates a lower boundary for the MM dimerization affinity, namely $K_d^{dimer} \gg 50$ μM in the presence of GTP. Further constraining of K_d^{dimer} was technically not feasible due to the required high MM concentrations (>50 μM) in the GTPase assay.

Running the GTPase assay beyond the linear regime allows GDP to compete with GTP for the active site. Therefore, the GTPase kinetics of such an experiment contains information on the relative affinity between GTP and GDP for the MM. A kinetic model was devised to fit experimental traces and determine unknown parameters (SI Section S1.1). Varying this setup with different initial conditions (Figure 2F) allowed us to estimate an apparent GTP on-rate of 6.6 $s^{-1}\mu M^{-1}$(Table 1), which was not straightforward to determine with mant-GTP (Figure S1).

Because of the low MM dimerization affinity, nucleotide kinetics within a dimer are difficult to examine, yet are required to understand the full catalytic GTPase cycle. To obtain these parameters at protein concentrations accessible to in vitro experiments, we engineered a Zn^{2+}-dependent metal bridge by introducing histidines in the G-interface (Figure S2A), a construct

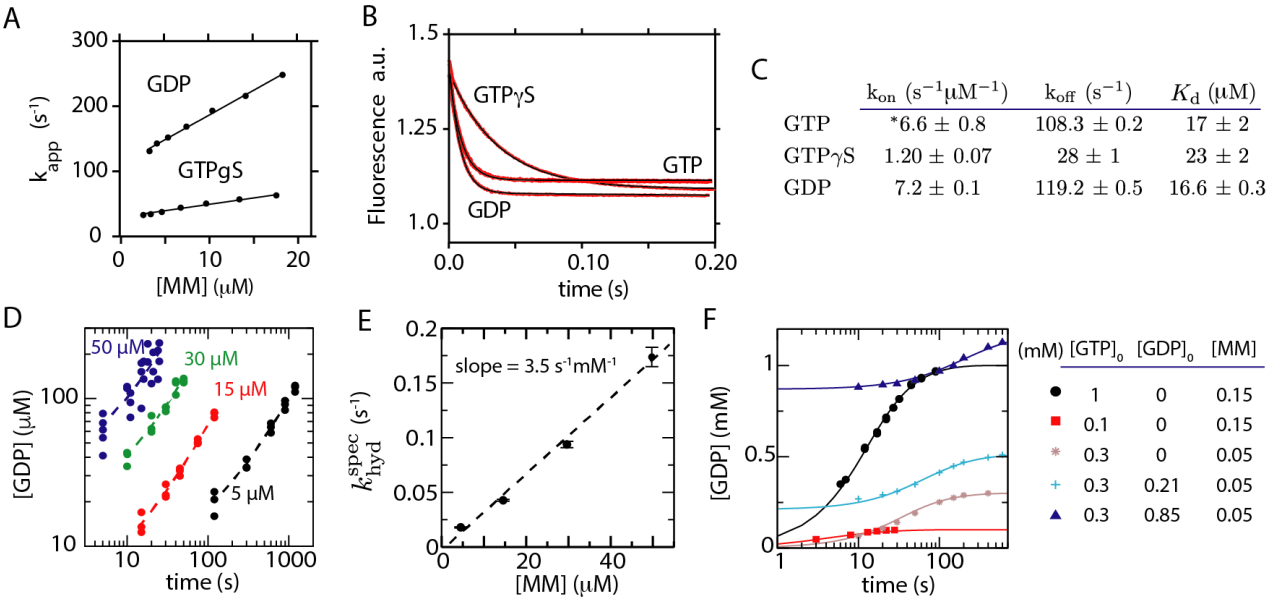

	k_{on} ($s^{-1}\mu M^{-1}$)	k_{off} (s^{-1})	K_d (μM)
GTP	*6.6 ± 0.8	108.3 ± 0.2	17 ± 2
GTPγS	1.20 ± 0.07	28 ± 1	23 ± 2
GDP	7.2 ± 0.1	119.2 ± 0.5	16.6 ± 0.3

Figure 2: Nucleotide binding kinetics and GTPase activity. A) Association rate constants are obtained from the slope of k_{app} versus MM concentration. See Figure S1 for GTP association curves. B) Nucleotide dissociation rates are measured by mixing with excess unlabeled nucleotide. C) Table of determined mant-nucleotide binding/dissociation rates of the MM construct. K_d is defined by the ratio k_{off}/k_{on}. *GTP on rate value is determined from kinetic modeling of GTPase activity (Panel F) because mant binding did not show a single exponential fluorescence increase (Figure S1). D) GDP production as a function of time in the linear regime for increasing concentrations of MM and an initial GTP concentration of 1 mM. Dotted lines are linear fits to three independent experiments. E) Slope from (D) divided by the protein concentration gives the specific hydrolysis rate (k_{hyd}^{spec}). Linear dependence of the specific hydrolysis rate on protein concentration indicates that GTPase activity is controlled by dimerization. F) Running the GTPase reaction beyond the linear regime for various initial conditions. Solid lines are the global least-squares fit between all measured points for a model that predicts k_{on} for GTP is 6.6 $s^{-1}\mu M^{-1}$. See Section S1.1 for the kinetic scheme.

termed MM-HH. We confirmed the correct G interface orientation of GDP-bound MM-HH dimers by crystal structure analysis (Figure S2A and Table S1). Stable assembly of the MM-HH construct in the presence of Zn^{2+} was demonstrated with size exclusion chromatography and FRET (Figure S2B,C).

Surprisingly, GTP and its analogs interfered with the formation of the Zn^{2+} bridge (Figure S2C-E), which precluded analysis of the dimer association kinetics. Regarding dissociation, GDP slowed the dimer dissociation rate of the Zn^{2+}stabilized MM-HH dimers six-fold relative to the apo state (Figure S2E), consistent with a long-lived post-hydrolysis dimeric state.

Relevant to nucleotide exchange, the association rates of mant-nucleotides to MM-HH in presence of Zn^{2+} were in line with the dissociation rate of the dimer, implying nucleotides could only bind to the monomer (Figure S2G-J). Similarly, the off rate for mant-GDP was 100-fold slower in the presence of Zn^{2+}, indicating that dimer dissociation should precede nucleotide dissociation in the catalytic cycle. Taken together, these kinetic results allow us to dissect the interplay between nucleotide binding and MM dimerization during the GTPase cycle (Figure 3).

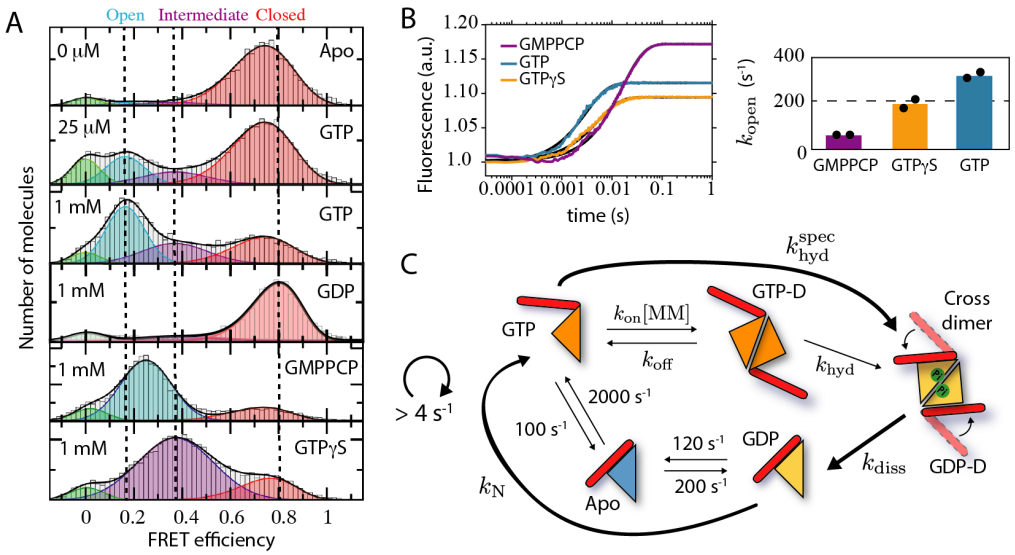

Figure 3: FRET measurements reveal the dependence of the G domain/BSE conformation on nucleotide state. A) smFRET histograms were fit to a four Gaussian state model and were colored according to the approximate position of the peaks: red, closed; purple, intermediate open; cyan, open; green, molecules lacking an active acceptor dye. Apo and GDP states are strongly peaked at high FRET while the other ligands show heterogeneity. The picomolar concentrations of MM used for smFRET ensured that the ensembles corresponded to MM monomers. B) Kinetics of opening are measured by mixing doubly-labeled MM with saturating concentrations (1 mM) of nucleotide. Single exponential fits to donor fluorescence are shown. Bar graph shows the opening rate determined by averaging the single exponential rate constants from two independent experiments (shown as black dots). The measured rate involves two processes: nucleotide binding and the conformational change. Although, since the binding rate at 1 mM GTP is much larger (6600 s^{-1}), the measured rate corresponds to the conformational rearrangement after GTP binding. C) GTPase cycle for the MM. Ligand binding kinetics are taken from Table 1 assuming physiological concentrations of 300 μM GTP and 30 μM GDP. [MM] refers to the concentration of GTP-bound MM. Experimental measurements of GTPase activity in the presence of membranes sets a lower limit of 4 s^{-1} [10] for the whole cycle.

Nucleotide-dependent motor module conformation in solution

To understand how GTPase cycles are coupled to force generation, the relationship between the conformational state of the MM and its nucleotide state must be quantified. To this end, we used single-molecule FRET (smFRET) to monitor the relative orientation of the G domain and BSE by introducing a pair of FRET dyes, one in the BSE and the other in the G domain (Figure 1D). Molecular simulations that included thermal fluctuations around the crystal structures including the dyes, provided estimates of the mean FRET efficiency of 0.19 and 0.79 for the open and closed structures, respectively (Figure S3).

The smFRET experiments were performed on freely diffusing MMs in the presence of various nucleotides (Figure 3A). In the presence of GTP, three populations were observed: a dominant open state with a FRET efficiency peak (E) at $E = 0.18$, an intermediate state at $E = 0.39$, and a closed state at $E = 0.77$. The peak values of the open and closed states were in excellent agreement with the predicted values (Figure S3). In contrast, the GTP analogs GMPPCP and GTPγS showed bimodal distributions. While both populated the closed state to a small degree, the lower FRET state dominated for both GTP analogs. Interestingly, the low FRET peak for GTPγS coincided with the intermediate peak found in the presence of GTP and

the low FRET peak for GMPPCP was positioned between the intermediate and open. Thus, different non-hydrolyzable GTP analogues produce different structural ensembles from those found with GTP and extreme care has therefore to be taken when interpreting experiments using GTP analogs. Remarkably, in the absence of nucleotide or in the presence of GDP, the conformational distributions were strongly shifted to the closed state. Without nucleotide, the position of the FRET peak coincided with the GTP-bound closed state. For GDP, the closed state was shifted slightly higher to $E = 0.8$. As detailed in the next section, a nucleotide state that induces a strong conformational preference, e.g. as seen for GDP, can be harnessed for converting conformational strain into mechanical work.

While the smFRET histograms provided an equilibrium description of the MM conformation, ensemble stopped-flow measurements were used to report on the relaxation rate between the equilibrium distributions. The opening rate, i.e. from apo (closed) to the GTP-bound state, was fit by a single exponential with a time constant of ≈ 300 s^{-1} (Figure 3B). The closing rate in solution induced by GTP dissociation is > 105 s^{-1} (Figure S3G). However, this value is less relevant to dynamin function since, in the filament, closing takes place within a dimer and under load.

Our kinetic and conformational results are summarized in a schematic of the GTPase cycle controlling motor function (Figure 3D). GTP-bound monomers are dominantly open (Figure 3A) and must dimerize (GTP-D) to activate hydrolysis (Figure 2E). Hydrolysis leads to a strong preference in the dimer (GDP-D) for the closed state. This is supported both by the smFRET GDP histogram (Figure 3A) and crystallography [14, 20]. The dimer in its GDP·Pi or GDP state dissociates only slowly, consistent with the high stability of MM dimers bound to GDP·AlF_4^- [14] and our kinetic results with GDP (Figure S2D). Dimer dissociation precedes nucleotide exchange (Figure S2I). Once monomeric, GDP exchanges in favor of GTP, which completes the cycle. Because relaxation to the open ensemble is fast (Figure 3B), e.g. compared to GDP dissociation, GTP binding and opening are taken as simultaneous in the GTPase cycle. Experimental measurements of GTPase activity in the presence of membranes have set a lower limit of 4 s^{-1} [10] for the whole cycle. The slowest measured rate in the forward direction is GDP dissociation at 120 s^{-1}, which sets an upper limit on the speed of the cycle. In the next sections we explore how this cycle drives force generation within a dynamin filament leading to motor activity.

Force generated by a single dimer motor

Within a helical dynamin filament, a pair of GTP-bound MMs belonging to adjacent rungs dimerize to form a link of length ℓ, i.e. the end-to-end distance of the dimer (Figure 4A). Upon hydrolysis, the equilibrium conformation of the dimer shifts from the open to the closed state, and thus, its equilibrium length gets shorter. However, if the filament is stalled, the actual length of the dimer cannot change, and hence a contracting force of magnitude $F(\ell)$ arises along the link. The force persists over the lifetime $1/k_{\text{diss}}$ of a dimer, i.e. until dissociation of the two MMs occurs.

The mean force required to stall a filament subjected to the forces of a single MM dimer averaged over many GTPase cycles, can be decomposed into the components $\langle F_s \rangle$ along the filament and $\langle F_t \rangle$ transverse to it, where $\langle\rangle$ indicates a time averaged quantity. The component

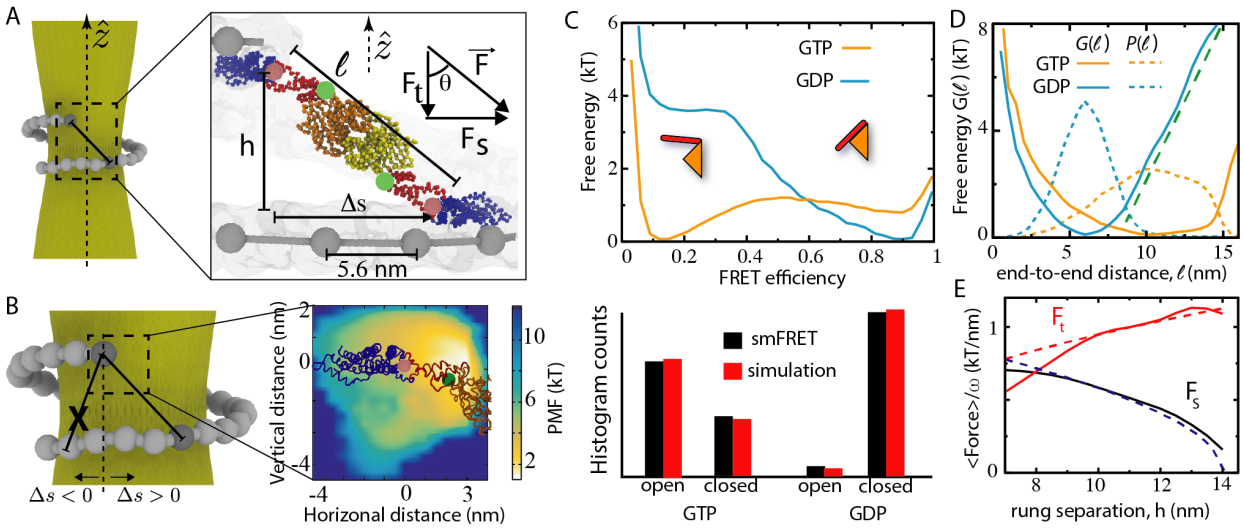

Figure 4: From conformational dynamics to force generation. A) An MM dimer forms a link between two neighboring filament turns. The link length ℓ is defined as the distance between the hinge 1 connections (pink circles). Green circles identify hinge 2. The displacement ℓ can be decomposed into the component Δs along the filament and the component h transverse to it. Similarly, the force F exerted on the upper filament by the cross-link can be decomposed into F_s and F_t. B) The structure of hinge 1 biases MM cross-dimers to be formed at positive Δs. Two-dimensional histogram in the z,s-plane of the position of hinge 2 (green bead) relative to hinge 1 (pink beak) in structure-based simulations indicates that, under thermal fluctuations, a MM in the upper rung is dominantly slanted toward the right. C) Dual-basin protein simulations for a single MM with the mixing weight set to reproduce the relative populations of low and high FRET for the GTP- and GDP-bound monomers (lower panel). Open and closed refer to FRET efficiency <0.5 and >0.5. Upper panel shows the resulting free energy as a function of the simulated FRET efficiency. D) Free energies as functions of ℓ for MM dimers constructed by connecting either two GTP-bound or two GDP-bound monomers via the G interface. Additionally, the corresponding probability distributions $P(\ell)$ are shown as dashed lines. The free energy of a GDP dimer is approximately linear (green dashed line for comparison) for $\ell > 8$ nm, so that the force $F = -dG/d\ell$ remains almost constant at $F_0 = 1.3$ k_BT/nm within this range. E) Average components of the stall force for a single motor along the filament and in the transverse direction. The force is averaged over many cycles of association/dissociation that are initiated over all allowed shifts Δs. Solid lines use the simulated distributions from (C), while the dashed lines show the approximate analytical results for a flat GTP distribution and a constant GDP force for $h < \ell < 14$ nm. The duty ratio ω is the mean fraction of the GTPase cycle within which a GDP-bound MM dimer stays formed.

$\langle F_t \rangle$ tends to pull the turns closer together, whereas $\langle F_s \rangle$ generates the torque; both of them depend on the separation h between the turns. Suppose that ω is the probability (often referred to as the duty ratio [33]) to find a MM in the dimerized state and $P(\ell)$ is the (conditional) probability that, if a cross-dimer is formed, it has length ℓ. Then, for a MM located in the upper turn and forming cross-dimers to the lower turn, the component of the mean force along the lower filament needed to stall is given by

$$\langle F_s \rangle = \omega \int_{\ell_{\min}}^{\ell_{\max}} P(\ell) F(\ell) \sin\theta(\ell) d\ell. \tag{1}$$

where θ is the slant angle (Figure 4A). The transverse component $\langle F_t \rangle$ is given by Eq.(1) with $\sin\theta$ replaced by $-\cos\theta$. The stall forces on the upper turn are reversed.

Importantly, if the formation of dimers slanted in both directions (i.e., with positive and negative Δs or angle θ) were equally probable, the force $\langle F_s \rangle$ would have averaged to zero.

Inspection of the available dynamin structures however shows that hinge 1 takes a preferred orientation (Figure S4), thus introducing a directional bias for the slants and a ratchet effect (Figure 4B). A hinge 1 in the upper turn prefers an orientation that slants the MM to the right and, by symmetry, slants to the left in the lower turn. Therefore, in our model, formation of dimers was only allowed at positive displacements ($\Delta s > 0$) along the filament.

In Eq.(1), $P(\ell) = P_{\mathrm{GTP}}(\ell)$ is the equilibrium distance distribution in pre-hydrolysis GTP-bound dimers. The contraction force is $F(\ell) = -dG_{\mathrm{GDP}}(\ell)/d\ell$ where $G_{\mathrm{GDP}}(\ell)$ is the Helmholtz free energy of a post-hydrolysis GDP-bound MM dimer. Note that this energy determines the equilibrium distribution $P_{\mathrm{GDP}}(\ell) \sim \exp(-G_{\mathrm{GDP}}(\ell)/k_B T)$ of distances in free GDP-bound dimers. Therefore, $F(\ell) = k_B T(d \ln P_{\mathrm{GDP}}(\ell)/d\ell)$.

We determined the distributions $P_{\mathrm{GTP}}(\ell)$ and $P_{\mathrm{GDP}}(\ell)$ from MD simulations of a dual-basin structure-based model of the MM dimer (see Methods for details). The MM dimer description was obtained by connecting two MM monomers, each described by the dual-basin model, at their G-interface. The weighting between the open and closed states' contributions to the monomeric energy potential was adjusted such that the simulated distributions matched the abundancies of open and closed states determined by smFRET (Figure 4C). Thus, although ℓ could not be directly tracked by experiment, the simulated dimer allowed us to calculate ℓ distributions that were consistent with the smFRET results.

The free energy profile $G_{\mathrm{GTP}}(\ell)$ of the GTP-bound monomer has two shallow minima corresponding to open and closed states (Figure 4C). Viewed along its FRET coordinate, the simulated dimer has three different states (open-open, open-closed, closed-closed (Figure S5)). In projection on distance ℓ, the free energy gets, however, flattened into a single broad basin (Figure 4D). According to Figure 4A, this implies that GTP-bound dimers can form over a wide range of ℓ and, therefore, over a wide range of filament displacements Δs. In contrast, the free energy $G_{\mathrm{GDP}}(\ell)$ for GDP-bound dimers has a single narrow minimum at a shorter distance ℓ (Figure 4D). Remarkably, the force generated by a GDP-bound dimer stays approximately constant at $F_0 = 1.3$ $\mathrm{k_B T/nm}$ over a range of ℓ from 8 nm to 14 nm. Note that the latter estimate is however sensitive to relative weights of the open and closed conformations in the GDP-bound MM. Since the observed frequency of the open conformation is likely enhanced by experimental noise, F_0 has to be viewed as a lower bound for the force.

The determined nucleotide-dependent distance distributions and Eq. 1 were used to estimate the mean force generated under the stall condition by a MM dimer motor as a function of h (Figure 4E). For a simple analytic estimate, a flat distribution $P(\ell) = 1/(\ell_{\mathrm{max}} - \ell_{\mathrm{min}})$ with $\ell_{\mathrm{min}} = h$ and $\ell_{\mathrm{max}} = 14$ nm and a constant force $F(\ell) = F_0$ was used. The force component $\langle F_s \rangle$ along the filament decreases with the separation h between the turns, whereas the transverse component $\langle F_t \rangle$ increases with it (Figure 4E). This is because the links get more aligned along the helical axis as h increases; no links are possible if the separation is too large. Note that the mean torque, locally applied to the filament by a MM dimer motor, is $F_s R$ where R is the filament radius. Assuming that a MM is found predominantly in the dimerized state (i.e. ω is near unity), F_s is 2.9 pN and the mean torque generated by a single motor in the non-constricted state (e.g., as in Figure 1C where $h = 8$ nm and $R = 25$ nm) is 72 pN·nm.

Collective action of dimer motors and constriction of membrane tube

Within a helical dynamin filament, many MM dimers can be formed, each generating a force. To address the question of how the collective action of such dimers produces constriction of the filament and, thus, of the membrane, the recently developed coarse-grained model of the dynamin filament interacting with a deformable membrane tube [24] was employed. This previous model was augmented to account for the motor activity of dynamin, and the motor forces were introduced in two ways. In the simplest average-force (AF) model, all MMs are assumed to operate independently and, moreover, each of them applies the same constant force to its neighboring filament (i.e., the average stall force of Figure 4E). In the more accurate explicit-force (EF) model, the formation and dissociation of individual MM dimers are resolved.

An important parameter is the duty ratio ω, which specifies the proportion of its GTPase cycle when a MM is producing force. In terms of the GTPase cycle kinetics (Figure 3D),

$$\omega = (k_{\text{diss}} T)^{-1}, \tag{2}$$

where $T = 1/k_{\text{hyd}}^{\text{spec}} + 1/k_{\text{diss}} + 1/k_{\text{N}}$ is the average cycle time and k_{diss} is the dimer dissociation rate. Since the duty ratio depends on experimentally inaccessible rates, namely on the hydrolysis rate $k_{\text{hyd}}^{\text{spec}}$ within the constrained environment of the filament and on the dissociation rate k_{diss}, we performed simulatons over a series of duty ratios ω varying between 0 and 1. In the AF model, the parameter ω enters directly as an overall scaling factor of the motor force (Eq. (1)). In the EF model, where the input parameters are rather the kinetic rates, ω was calculated by Eq. (2).

In the AF model, each MM applied the average stall forces presented in Figure 4E to its neighboring filament. The balance between the elastic expansion force of the membrane and the constriction forces generated by the motors determined the steady-state membrane constriction. The constriction force was sufficient to produce an inner lumen radius (ILR) under 1 nm in the steady state of the AF model (Figure 5A), less than the threshold for spontaneous hemi-fission ($\lesssim$2 nm [25]). As could be expected, larger duty ratios resulted in more strongly constricted filaments.

In the EF model, MM dimers were explicitly introduced into the coarse-grained filament description [24] as elastic cross-dimers that connected the beads representing stalk domains and applied forces between them. Since each bead corresponds to a dynamin dimer, it had two MMs associated with it (Figure S6A). The nucleotide state of each MM was tracked and the GTPase cycle (Figure 3D) was implemented within it. Dimerization, i.e. formation of a cross-dimer, could occur if both MMs were GTP-bound. After the hydrolysis-induced conformational change, the cross-dimer became strained and produced a contracting force between the pair of connected beads. The MM dimers dissociated at rate k_{diss} (see Methods for details).

The steady-state ILRs at different duty ratios ω obtained in 40-bead EF model simulations are displayed in Figure 5A. As in the AF model, strong constriction was observed at sufficiently high duty ratios ω (Supplementary Video 1). Shortening the filament reduced constriction, while increasing its length beyond 40 dimers had little effect (Figure 5B). Increasing the lower-limit estimate of the contraction force F_0 by 50% further decreased the ILR (Figure 5B). Note that at similar duty ratios, simulations of the EF model yield larger ILRs as compared to the AF model. This is because, in the EF model, the crowded environment within the

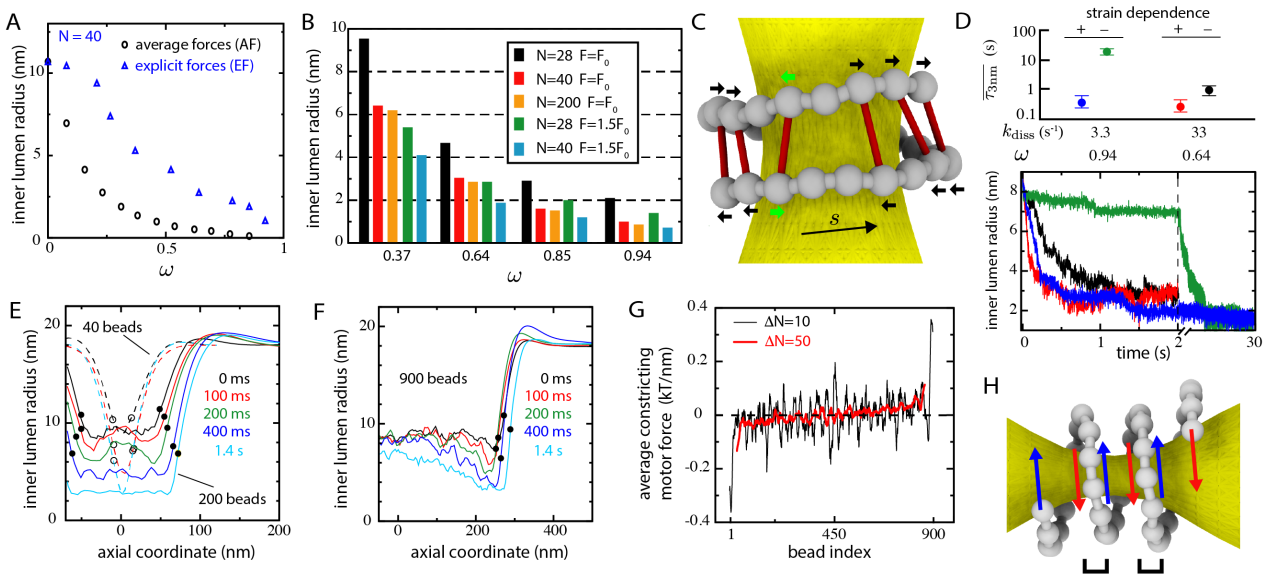

Figure 5: Collective motor activity and membrane constriction. A) Comparison of the steady-state inner lumen radii (ILR) for a membrane tube with the stiffness of 24 k_BT and the tension of 0.03 k_BT/nm^2 in the AF (circles) and EF (triangles) models as functions of the duty ratio ω for the filaments with 40 dimers. Refer to Figure S7 for an explanation of the discrepancy between the two models. The membrane radius is measured from the axis to the center of a 4 nm wide bilayer, hence the ILR is less than the membrane radius by 2 nm. B) Dependence of the steady-state ILR on the filament length and the motor force in the EF model. C) Example of a configuration including a blocking link (with green arrows). Formed GDP-bound MM dimers are indicated by red lines. D) Constriction in the EF model is much accelerated under a strain-dependent dissociation rate (green and black: strain-independent $k_{\rm diss}$, blue and red: strain-dependent $k_{\rm diss}$). (top) Average times $\overline{\tau_{3\ \rm nm}}$ to reach an ILR of 3 nm; horizontal bars indicate the upper and lower quartiles over 50 constriction simulations. (bottom) Examples of time dependence of the ILR (the same color code as above). E) Evolutions of membrane inner radius profiles for the filaments with 40 (dashed) and 200 (solid) beads in the EF model with strain-dependent $k_{\rm diss}$ and $\omega = 0.94$ F) Evolution of membrane profiles in the same model for a filament with 900 beads. In E and F, circles mark the positions of terminal filament beads; all simulations started from the thermal equilibrium state in absence of GTP. G) Net local motor forces acting on the filament along its direction. The curves are running means over $\Delta N = 10$ (black) or $\Delta N = 50$ (red) beads averaged additionally over the first 500 ms of the EF simulation in panel F. H) Motor forces in the interior cancel each another because the neighboring turns pull the filament in opposite directions (brackets pair the forces).

filament prevents some MM cross-dimers from being formed for steric reasons, which reduces the constriction efficiency (Figure S7).

As the filament turns slide past one another during constriction, blocking MM dimers with $\Delta s < 0$ can develop (see Figure 5C and Supplementary Video 1). The blocking dimers produce forces acting in the opposite direction, thus tending to prevent further constriction. In analogy to the actomyosin system, where key kinetic steps are sensitive to strain [34–37], we explored how similar strain regulation would influence the motor operation of dynamin. Specifically, the dissociation of MM dimers can be affected by the strain because of the asymmetry of hinge 1. If the sign of the displacement Δs, characterizing the strain, is negative, dissociation of such blocking dimer may rapidly take place.

To this end, we implemented a hypothetical strain-dependent dimer dissociation rate $k_{\rm diss}$ in the EF model by introducing immediate dissociation of MM dimers upon $\Delta s < 0$. In EF simulations for a 40-bead filament and $k_{\rm diss} = 3.3\ {\rm s}^{-1}$, tight constriction below 2 nm was found

to occur already within 200 ms with the strain dependence, whereas this time increased to more than 10 s in absence of it, i.e. when blocking was allowed (Figure 5D and Supplementary Video 2). Under strain control, the constriction speed becomes limited not by MM dimer dissociation, but by other kinetic steps of the cycle, such as hydrolysis ($k_{\mathrm{hyd}}^{\mathrm{spec}}$) or nucleotide exchange (k_{N}) (see SI section S1.2 for a discussion of $k_{\mathrm{hyd}}^{\mathrm{spec}}$). Thus, k_{diss} could be decreased to maximize the duty ratio ω (Eq. 2) without penalizing the constriction speed. Note, the introduction of strain dependence of k_{diss} only affected the transition rate to the steady state, and thus, the dependence of the ILR on ω remained the same as in Figure 5A).

Finally, we studied the shape evolution of membrane tubes subjected to motor activity for filaments of various lengths (Figure 5E,F). During the evolution and in the steady state, tubes with short filaments (Figure 5E) are most constricted in the middle, where fission would thus preferentially take place too. In contrast, a long filament strongly constricts the membrane near its ends (Figure 5F and Supplementary Video 3). While the deformation later propagates towards the center and would eventually get uniform in the steady state, for long filaments fission can already occur earlier at one of the filament's ends. Note that motor forces within a long filament almost balance each other (Figure 5G) where the filament has two neighboring turns applying opposite forces (Figure 5H). Such cancellation is absent for the terminal turns and, thus, only the motors on the flanks of a long helical filament apply a net torque and contribute to constriction of the membrane.

Discussion

We have combined biochemical experiments and modeling to characterize the motor function of dynamin and its role in the remodeling of membranes. Stopped-flow and smFRET experiments have been employed to determine rate constants of the catalytic cycle and energetic parameters of the power stroke. These data have been used together with the known geometries of the dynamin motor module and the dynamin helix to build a coarse-grained model of active dynamin filaments on deformable membrane tubes. The model explicitly resolved GTPase-dependent cross-dimers between the filament turns.

We find that dynamin constriction is based on synergetic activity of its MMs, with conformational changes in cross-dimers driving neighboring turns of the filament to move relative to one another. By smFRET and MD simulations, we have demonstrated that, in the GDP-bound state, a MM dimer becomes shorter than in the GTP-bound state. Because the dimers form slanted links between neighboring turns, shortening of them creates a torque that pulls the turns relative to one another. Remarkably, nucleotide-dependent conformational changes (and thus the generated forces) in dynamin were much more pronounced than in the structurally similar MxA protein [38]. Whereas for MxA the ratio of populations of the open to closed states in the presence of GDP was 0.43 (i.e., 30% to 70%), the GDP-bound open state was practically undetectable for dynamin. This strong shift in the conformational state of the dynamin MMs singles out the power stroke as underlying the molecular motor mechanism for dynamin. Moreover, it highlights the functional difference with MxA, an antiviral machine likely acting on viral nucleocapsids rather than binding to membranes [39].

An important role in force generation is additionally played by the ratchet property of

hinge 1 connecting a MM to the stalk (Figure 4B). This property provides a directional bias for the slanted cross-dimers. Future experimental work toward uncovering the conformational ensemble of hinge 1 will be important not only for quantifying the ratchet – it can also lead to better understanding of the proposed strain dependence of the motor dimer dissociation rate. If the strain builds up and acts to accelerate the breakup of the G-domain interface of a blocking dimer, it should be transduced by hinge 1. The conceptual analog in the actomyosin system is the asymmetry within the myosin V lever arm and its role in speeding ADP release when the lever arm is pulled toward actin's plus-end [34, 40]. Although the hypothetical strain dependence offers clear functional benefits for dynamin, it should be also noted that, even in its absence, there are parametric regimes where strong constriction could be observed in under a second (Figure 5D).

By incorporating the GTPase-cycle kinetics and the MM dimer forces into the elastic description of dynamin filaments on deformable membrane tubes, a model for collective membrane constriction by MMs of dynamin was obtained. Its simulations showed gradual tube constriction until a steady state was reached. A principle conclusion was that tight constriction required the cooperation of many MMs, i.e. high duty ratios, implying the majority of MMs should be dimerized at any time. Operation of MMs was mostly asynchronous and independent. Nonetheless, through strain build-up and passive excluded-volume interactions, correlations between the motors could arise.

Parallels can be drawn between dynamin and the motor operation of myosin in the muscle [33, 37]. Apart from dynamin's helical shape and its unique combination of both filament and motor into a single protein, the arrangement of interacting G domains between neighboring turns of the helical filament (Figure 1C) is reminiscent of muscle myosin, where a straight thick filament formed by myosin II runs along a linear thin filament made by actin [33]. Many myosin heads can simultaneously bind to the thin filament and apply force. The force is generated through conformational changes of the myosin head and neck domain, analogous to the G domain and BSE in dynamin's MM.

Our presented motor-driven constriction mechanism is not contradictory to previous suggestions of a two step scission process, involving an assembly-based constriction followed by a final GTPase-dependent scission [9, 12, 26, 41]. Rather we show how the initial constriction step is also accomplished in a GTPase-dependent manner. While passive constriction during initial filament assembly can play a role, given dynamin's propensity for GTPase activity, as soon as a full turn of dynamin is assembled the motor activity will initiate. Furthermore, while the generated torque appears capable of promoting hemi-fission through constriction alone, we cannot discount that the PH domain additionally plays an active role during scission [9, 12, 26, 41]. It should be stressed that the final scission event was not reproduced in our simulations, whose aim was rather to show how dynamin generates and maintains tight membrane necks. To describe a further transition to hemi-fission and scission would have required more precise modeling of the membrane. While modeling, additional simplifications were made. The dynamin filament was treated as an elastic ribbon whose local orientation with respect to the membrane remained fixed, even though it had been noticed that tilt deformations changing the orientation might additionally contribute to the breakup [42]. Moreover, axial symmetry of the membrane was assumed.

The principal experimental features of membrane constriction by dynamin are either explained by our study or consistent with its results. We found that short dynamin helices consisting of 1.5 to 2 turns are sufficient to produce tight constriction [43]. Dynamin's ability to produce torque over a long dynamin helix [44] arises from repeated cycles of interaction between neighboring MMs (Supplementary Video 3). The fission at the edge of a dynamin coat, observed in the experiments with fluorescent membrane tubes pulled from giant unilamellar vesicles [16] or for nanotubes imaged by high-speed atomic force microscopy [45], can be readily explained by our model where the strongest constriction first develops near the filament ends. Furthermore, the fastest dynamin scission events are known to take approximately 100 ms [46], in agreement with the rapid constriction found in our simulations under the suggested strain dependence of the MM dimer dissociation rate. In summary, using an integrative experimental and theoretical approach, we have deciphered the molecular motor mechanism of dynamin that underlies its GTPase-driven role in membrane constriction and scission.

Acknowledgements

This work was supported by the European Research Council, ERC-2013-CoG-616024 (O.D), a grant of the German Research Foundation (Collaborative Research Grant 740, From Molecules to Modules) to O.D., by the Japanese Society for Promotion of Science (Grant-in-Aid for Scientific Research (C) 19K03765 to A.M), and through a Humboldt Foundation fellowship to J.N. H.H. thanks the Benoziyo Fund for the Advancement of Science, the Carolito Foundation, the Gurwin Family Fund for Scientific Research, the Leir Charitable Foundation, and the Koshland family. The work was further supported by the Irving and Cherna Moskowitz Center for Nano and Bio-Nano Imaging at the Weizmann Institute of Science. Diffraction data have been collected on BL14.1 at the BESSY II electron storage ring operated by the Helmholtz-Zentrum Berlin. We would particularly like to acknowledge the help and support of Manfred Weiss during the experiment.

Materials and methods

Cloning, expression, and purification

The pET-M11 vector was used to express a codon-optimized His6-tagged GTPase-BSE (MM) construct (Eurofins, residues 6-322 fused to residues 712-746 with a GSGSGS linker) in BL21 (DE3) Rosetta 2. Cells were grown at 37 °C to an OD600 of 0.4 and the protein was expressed in the presence of 0.15 mM IPTG overnight at 25 °C in TB medium, supplemented with 34 µg/ml of chloramphenicol and 50 µg/ml of kanamycin. Cells were harvested by centrifugation, resuspended in buffer A (20 mM HEPES-NaOH, pH 7.5, 500 mM NaCl, 15 mM imidazole, 5% glycerol) and lysed in a micofluidizer. The cleared lysate after centrifugation was incubated for 30 min with 5 ml Ni-NTA resin at 4 °C on a rocking platform. Afterwards, Ni-NTA beads were washed in batch 3 times with buffer A and transferred into a gravity-flow 20 ml column. Column material was further washed with 10 column volumes (CV) of buffer A supplemented with 2 mM ATP and 5 mM $MgCl_2$ and then with 2 CV of buffer A containing 50 mM imidazole. Eventually, the protein was eluted with 5 CV of buffer A containing 250 mM imidazole. The His6 tag was cleaved by incubation with TEV-protease during overnight dialysis against buffer A without imidazole. Subsequently, the protein was re-applied to the Ni-NTA column, collected in the flow-through fraction, and further purified via size-exclusion chromatography on a S200 26/600 Superdex column with running buffer C (20 mM HEPES-NaOH, pH 7.5, 150 mM NaCl). Fractions containing the pure protein were pooled, concentrated to 30-50 mg/ml, aliquoted and shock frozen in liquid nitrogen. The MM wild-type construct as well as various mutant variants were purified following the same protocol.

Mutagenesis and design of histidine mutants

For protein labeling with Alexa fluorophores or for experiments exploring metal-mediated dimerization of the MM constructs, the following mutations were introduced individually or in combination: T165C, R318C, N112C, K142H, N183H. Point mutations in the MM construct were introduced using QuickChange site-directed mutagenesis (Agilent). Cysteine mutations were used for covalent attachment of Alexa Fluor dyes and their locations were chosen to avoid any obvious functional interaction. The T165C mutation in combination with K142H, N183H was used to monitor formation of the Zn^{2+}stabilized dimer. The combination R318C (BSE) and N112C (G domain) was used to monitor the conformational change.

Analytical SEC analysis

To characterize Zn^{2+}-mediated dimerization of single- or double-histidine mutants of the MM, SEC was performed on a Superdex S200 column 10/300 GL equilibrated with buffer D (20 mM HEPES-NaOH, pH 7.5, 150 mM NaCl, 5 mM KCl, 0.2 mM $ZnSO_4$). For complex formation, 10-15 µl of the corresponding protein variant was mixed with buffer D. Following incubation on ice for 10 min, 100 µl of a 4 mg/ml solution was applied to SEC.

Protein crystallization and structure determination

For crystallization, MM-HH (MM with mutations K142H, N183H) dimer at 12 mg/ml was mixed in a 1:1 ratio with reservoir solution containing 0.1 M Tris-HCl, 0.25 M KBr, 30% (w/v) PEG MME 2000. Crystals were grown by sitting drop vapor diffusion at 20 °C. A dataset was collected from a single cryo-cooled crystal at BESSY synchrotron beamline BL14.1 (Berlin, Germany). Diffraction data to a maximal resolution of 2.0 Å were included for processing by the XDS software package [47]. The structure was solved by molecular replacement using the coordinates for GTPase-BSE of PDB entry 5D3Q using Phaser [48] within the software package Phenix [49]. Refinement and model validation were performed with Phenix. Model building was performed manually with COOT [50]. Six zinc ions were located based on the coordination spheres and positive difference densities after placement of water molecules at these positions. The model was deposited in the PDB database under accession number 6S9A.

Protein labeling with fluorescent probes

Thiol-reactive fluorescent dyes (ThermoFisher Scientific) were used for site-specific labeling of cysteines in MM variants. Using AlexaFluor 488 as donor and AlexaFluor 594 as acceptor provides a Föster distance of 5.4 nm [51, 52]. The T165C variant was used to determine the dissociation constants of the artificial dimer and the R318C/N112C double mutant for smFRET measurement. To reduce cysteines, 250 µl of a protein solution at 30 to 40 mg/ml was incubated with 20 mM DTT for 1 h on ice, following DTT removal by gel filtration on a S200 10/300 column equilibrated with buffer F (20 mM HEPES-NaOH, pH 7.5, 5 mM $MgCl_2$, 150 mM NaCl, 10 mM KCl). The concentrated proteins were mixed with the corresponding thiol-reactive dye in a 1:2 molar ratio (protein:dye) and incubated for 1 h at room temperature (RT). In case of double labeling by Alexa Fluor 488 and 594, the reaction was started with addition of Alexa Fluor 488 to the protein solution in a 1:0.66 (protein:dye) molar ratio. After 40 min of incubation at RT, Alexa Fluor 594 dye was added in a 1:2 (protein:dye) molar ratio and the reaction was continued for 1 h at RT. The labeling process was terminated by the addition of 10 mM DTT. After 5 min incubation at RT, insoluble material was removed by centrifugation and the sample was applied to a second round of SEC to remove unreacted dye and DTT. Labeling efficacy was calculated according to the manual of Thermo Fisher Scientific; a typical range was 90-100%. All fluorescence-based functional and GTP hydrolysis assays for the monomeric form of the MM constructs were performed in buffer 1 (20 mM HEPES-NaOH, pH 7.5, 150 mM KCl, 4 mM $MgCl_2$). Experiments with the artificially dimerized form of the MM-HH variant were performed in buffer 2 (20 mM HEPES-NaOH, pH 7.5, 150 mM KCl, 4 mM $MgCl_2$, 160 µM $ZnSO_4$). All experiments were carried out at RT if not otherwise stated.

Single-molecule FRET

Single-molecule FRET experiments were performed with a MicroTime 200 confocal system (PicoQuant, Germany) equipped with an Olympus IX73 inverted microscope and two pulsed excitation sources (40 MHz) controlled by a PDL 828-L "Sepia II" (PicoQuant, Germany). Pulsed Interleaved Excitation (PIE) [53] was used to identify molecules with active acceptor and donor dyes. Two light sources, a 485 nm Diode Laser (LDH-D-C-485, PicoQuant) and

a white-light laser (Solea, PicoQuant) set to an excitation wavelength of 595 nm were used to excite the donor and the acceptor dyes alternatingly. The laser intensities were adjusted to 100 μW at 485 nm and 30 μW at 595 nm (Pm100D, Thor Labs). The excitation beam was guided through a major dichroic mirror (ZT 470-491/594 rpc, Chroma) to a 60x, 1.2NA water objective (Olympus) that focuses the beam into the sample. The sample was placed in a home made cuvette with a volume of 50 μl (quartz 25 mm diameter round cover slips (Esco Optics), borosilicate glass 6 mm diameter cloning cylinder (Hilgenberg), Norland 61 optical adhesive (Thorlabs)). All measurements were performed at a laser power of 100 μW (485 nm) and 30 μW (585 nm) measured at the back aperture of the objective. Photons emitted from the sample were collected by the same objective and after passing the major dichroic mirror (ZT 470-491/594 rpc, Chroma), the residual excitation light was filtered by a long-pass filter (BLP01-488R, Semrock) and sent through a 100 μm pinhole. The sample fluorescence was detected with two channels. Donor and acceptor fluorescence were separated via a dichroic mirror (T585 LPXR, Chroma) and each color was focused onto a single-photon avalanche diode (SPAD) (Excelitas) with additional bandpass filters: FF03-525/50, (Semrock) for the donor SPAD and FF02-650/100 (Semrock) for the acceptor SPAD. The arrival time of every detected photon was recorded with a HydraHarp 400M time 9 correlated single photon counting module (PicoQuant) and stored with a resolution of 16 ps.

Photons from individual molecules, separated by less than 100 μs were combined into bursts if the total number of photons exceeded 30. Photon counts were corrected for background, acceptor direct excitation, and different detection efficiencies of the individual detectors. A PIE stoichiometry ratio $S < 0.7$ was used to identify molecules with an active acceptor. Identified bursts were corrected for background, differences in quantum yields of donor and acceptor, different collection efficiencies in the detection channels, cross-talk, and direct acceptor excitation. FRET histograms were fitted with a combination of Gaussian functions as previously described.

The labeled MM construct was diluted to a concentration of approximately 50 pM in 20 mM HEPES-NaOH, pH 7.5, 150 mM KCl, 4 mM $MgCl_2$ in the absence or presence of increasing amounts of GTP, GTPγS, GMPPCP, GDP. To prevent surface adhesion of the protein and to maximize photon emission, 0.001% Tween 20 (Pierce) was included in the buffer. All measurements were performed at 23 °C.

In the presence of saturating concentrations of GTP and GTP analogs (> 1 mM, see Figure S3E), a significant closed population remained, which could not be fully explained by unbound MM (predicted to < 2% based on the determined affinities) or GDP contamination. The purity of GTP was 99.4% and of GTPγS was 95%, as determined by HPLC.

Stopped-flow kinetic measurements

All fast kinetic measurements were carried out on Chirascan stopped-flow accessory unit equipped with an independent LED power source (Applied Photophysics). For nucleotide binding studies, fluorescent 2'(3')-O-(N-methylanthraniloyl) (Mant)-substituted nucleotides were used. The dye fluorescence was excited at 350 nm and the fluorescence change monitored through a Schott 395 nm cut-off filter. In order to measure k_{on} values, increasing concentrations of MM construct (2, 3, 4.5, 7, 10.5, 15 and 20 μM) were titrated with 1 μM mant-nucleotide. For each concen-

tration, at least 5 traces originated from the same sample were averaged. A linear regression was performed and the slope provided k_{on} with error given by the standard deviation in the slope. For quenching experiments to measure k_{rmoff}, 20 μM protein and 1 μM mant-nucleotide were mixed with 500 μM GTPγS or GDP. Three independent experiments were performed. Rates were determined by single exponential fits and the presented rate represents the average over the three experiments and the error the standard deviation. Error in K_{d} is determined by propagating the errors in k_{on} and k_{rmoff}.

In order to detect conformational changes in the MM construct, FRET between Alexa Fluor 488 and 596 fluorescent pairs was recorded. Signals from both dyes were simultaneously detected using two photomultiplier tubes and a Chroma ET525/50m band-pass and Schott 645 nm cut-off filter. G domain/BSE opening was performed by mixing 5 μM of protein and 500 μM of GTPγS. Experiments for measuring G domain/BSE closure were performed as follows: 5 μM protein and 100 μM GTPγS were mixed with 2 mM GDP, where GDP will outcompete GTPγS for binding to the protein. Concentrations of reactants in both syringes of all stopped-flow experiments were two times higher compared to the measurement cell since they were diluted upon mixing in 1:1 ratio. Throughout the manuscript, indicated concentrations are those after mixing.

Zn^{2+}-dependent MM dimerization

For determining the concentration of Zn^{2+} required to promote dimerization, MM-HH(K142H, N183H) including T165C was separately labeled via Cys165 with either Alexa Fluor 488 or 594 dyes. The labelled proteins were mixed in a 1:2 molar ratio (Alexa Fluor 488: Alexa Fluor 594) in 20 mM HEPES-NaOH, pH 7.5, 150 mM KCl, 4 mM $MgCl_2$. In order to measure Kd values, 5 μM of the labelled protein mixture was incubated with different concentrations of $ZnSO_4$ (177.8, 118.5, 79.0, 52.7, 35.1, 23.4 and 15.6 μM) and incubated for 10 min on ice. The resulting FRET signal was recorded on a Teacan1000pro plate reader (λ_{ex}= 465 nm and λ_{em}=616 nm).

To account for $ZnSO_4$-mediating quenching effects on the AF488 dye, a correction factor was calculated: the fluorescence intensity of AF488-labeled protein in the absence of $ZnSO_4$ was divided by the fluorescence value in the presence of each particular $ZnSO_4$ concentration. Subsequently, the background FRET signal in the protein sample without $ZnSO_4$ was subtracted from each measured and corrected data point. FRET data were plotted against $ZnSO_4$ concentration. The titration indicated that dimerization saturated near 200 μM Zn^{2+}.

In order to evaluate the effect of nucleotide on dimerization, the same type of experiments were performed in the presence of 160 μM Zn^{2+} and 0.5 mM GTPγS or GDP. To exclude an influence of $MgCl_2$ on dimerization, additional experiments were performed in the absence or presence of 2 mM $MgCl_2$.

GTPase assay

GTPase assays were performed in 20 mM HEPES-NaOH, pH 7.5, 150 mM KCl, 4 mM $MgCl_2$ containing 5 μM of the MM construct and 1 mM GTP. The reaction carried out at 37 °C. Upon starting the reaction, 2 μl reaction aliquots were withdrawn at different time points and mixed with 2 μl of 1 M HCl to stop the reaction and then diluted with 26 μl of HPLC buffer (100 mM

potassium phosphate buffer, pH 6.5, 10 mM tetrabutylammonium bromide, 7.5% acetonitrile). Reaction products were quantified on an HPLC system from Agilent equipped with a Hypersil ODS-2 C18 column (250 × 4 mm). Each time point measurement (5 time points) was done in triplicate with the same sample. Specific hydrolysis rate for each protein concentration was computed by linear regression with error given by the standard deviation of the linear fit. To investigate the effect of Zn^{2+} on artificial dimer activity, 2.5 μM, 10 μM, 40 μM, 80 μM, 160 μM and 400 μM $ZnSO_4$ was added to the standard reaction. For testing concentration-dependent GTPase activity, reactions were performed in standard buffer at RT with 5, 15, 30 and 50 μM enzyme. Competition GTPase assay were performed by adding 0.21 or 0.85 mM of GDP to the reactions. See SI Section S1.1 for detail of the kinetic modeling of the competition assay.

Molecular dynamics simulations

The conformational dynamics of the MM were studied with "structure-based models" (SBMs), a class of simplified model that is commonly used to investigate protein folding. The model is referred to as structure-based because the global minimum of the energy function is assigned based on a crystallographic structure. In this model, electrostatics and solvation effects are implicitly accounted for, insofar as the stabilizing interactions in the model describe the effective residue interactions after averaging over all the myriad interactions that stabilize a particular crystal configuration. For our purposes here, SBMs are particularly well suited because the open and closed MM configurations have both been crystallized. Importantly, (single-basin) structure-based molecular dynamics simulations of the monomeric MM based on either the GMPPCP crystal structure (open) or the GDP crystal structure (closed) yielded FRET levels for the open and closed states that were similar to those observed in smFRET (Figure S3). Additionally, the simplified energetics of SBMs allowed a straightforward matching to experimentally-measured distributions.

We should note that the smFRET histogram for GTP-bound MM appears to possess an intermediate state (Figure 3A), although a two-state fit with skewed Gaussians is reasonable too. The fact that GTPγS populates an open state peaked at the same FRET level as this GTP intermediate state provides further evidence that such an intermediate state might exist. While we have not included into the model this intermediate state, for our purposes here, such an intermediate within GTP-bound dimers would have little effect, only serving to further flatten the already flat ℓ distribution.

A dual-basin structure-based model was constructed, meaning that both the open and closed MM structures were explicit energetic minima. The open structure was defined by chain A of the GMPPCP-bound MM (S_O) [15] and the closed structure by chain A of the GTP-bound MM (S_C) [20]. The G domains between the two structures are nearly identical. The structural differences mainly reside in the positioning of the first BSE helix relative to the G domain (Figure S5). The native configuration for the loop connecting the second and third BSE helices (which was unresolved in the crystal structures) was taken as the hinge 1 configuration in the tetramer crystal structure with a 3.8 Å bond inserted between Pro322 and Glu716.

We followed the general approach described here [54] in defining the dual-basin potential with two alterations: 1) a Gaussian shaped native contact interaction that can have two minima was used [55], and 2) angle and dihedral interactions differing between the structures by more

than a certain cutoff were removed. Briefly, the native contact maps [56], i.e. those residues that are close in the native structure, were divided into three contact maps (M): unique contacts only in 1) S_O (M_O^U) or 2) S_C (M_C^U) and 3) shared contacts that were in both structures (M^S). All native contacts were given a stabilizing interaction centered at the native distance, the shared contacts had a minimum at both distances. Bond angles between three sequential residues and dihedral angles were considered frustrated and not given stabilizing interactions if the angles differed by more than 20° or 30°, respectively. The remaining angles were biased toward the average angle between the S_O and S_C.

It is important to point out that the specific construction of the dual SBM is unlikely to influence the presented results since experimental information was used to calibrate the energetics of the model. The simulation results of main interest are 1) the shapes of the force versus extension curves for GTP-bound and GDP-bound MM dimers and 2) validation of open and closed crystal structures for describing smFRET data. These results are geometrical features that are not sensitive to the details of the potential.

Simulations were performed using GROMACS 4.5.3 [57] containing code edits implementing Gaussian contact interactions (available at http://smog-server.org). Single basin simulation topologies were generated using the SMOG2 software [58] with the forcefield "SBM_CAgauss" and combined using an in-house script. The temperature (T=0.92 in reduced units) was chosen such that the average C_α atom RMSD in the closed MM agreed between a 100 ns explicit solvent simulation using AMBER99SB-ILDN at 310K and the SBM. Assuming this equivalence, the simulation unit k_BT corresponds to 4.3 pN/nm. The temperature was maintained with stochastic dynamics with coupling constant 0.1 and the time step was 0.0005.

The energy potential was

$$\begin{aligned} V_{\text{dual}}(\alpha) &= \sum_{ij\in\text{bonds}} \epsilon_{\text{b}}(r_{ij}-r_{ij}^{\text{C}})^2 + \sum_{ijk\in\text{angles}} \epsilon_\theta \left(\theta_{ijk} - \tfrac{\theta_{ijk}^{\text{C}}+\theta_{ijk}^{\text{O}}}{2}\right)^2 + \sum_{ijkl\in\text{dihedrals}} \epsilon_\phi F_{\text{D}} \left(\phi_{ijkl} - \tfrac{\phi_{ijkl}^{\text{C}}+\phi_{ijkl}^{\text{O}}}{2}\right) \\ & \sum_{ij\in M_{\text{C}}^{\text{U}}} N_{ij}(\alpha\epsilon_{\text{N}}, r_{ij}^{\text{C}}) + \sum_{ij\in M_{\text{O}}^{\text{U}}} N_{ij}(\epsilon_{\text{N}}, r_{ij}^{\text{O}}) + \sum_{ij\in M^{\text{S}}} N_{ij}(\epsilon_{\text{N}}, r_{ij}^{\text{C}}, r_{ij}^{\text{O}}) + \sum_{ij\notin contacts} \epsilon R_{ij} \end{aligned}$$

where α allowed the weight of closed states versus open states to be modulated. Superscript O and C denote that the value is taken from either the open or closed crystal structure. F_{D} is a typical dihedral-like potential

$$F_{\text{D}}(x) = (1-\cos x) + 0.5(1-\cos 3x)$$

and N_{ij} is a native contact interaction consisting of a Gaussian well G_{ij} coupled a r^{-12} repulsion R_{ij} in such a way that fixes the minimum at (r_0, ϵ) [59].

$$N_{ij}(\epsilon, r_0) = \epsilon[(1+(1/\epsilon)R_{ij})(1+G_{ij}(r_0))-1]$$

with

$$G_{ij}(r_0) = -e^{(r_{ij}-r_0)^2/2\sigma^2}$$

and

$$R_{ij} = (a/r_{ij})^{12},$$

where $a = 4$ Å sets the bead excluded volume. The dual minimum contact interaction was similarly constructed,

$$N_{ij}(\epsilon, r_0^1, r_0^2) = \epsilon[(1+(1/\epsilon)R_{ij})((1+G_{ij}(r_0^1))(1+G_{ij}(r_0^2)))-1]$$

The values of the energetic parameters are $\epsilon_{\rm b} = 20000\epsilon$, $\epsilon_\theta = 40\epsilon$, $\epsilon_\phi = \epsilon$, $\epsilon_{\rm N} = \epsilon$, where ϵ is the reduced energy unit.

To model more closely the distance measured during smFRET, explicit dyes were attached at T165C and R318C. The dye consisted of a linear chain of 6 C_α beads connected by bonds 3.8 Å in length (Figure S3D). The FRET efficiency for each snapshot was calculated based on $E = (1 + (d/d_0)^6)^{-1}$ using the distance d between the two terminal dye beads and $d_0 = 5.4$ nm (see also Figure S3). To compute the estimated FRET expected in either the open or closed ensemble including thermal fluctuations (Figure S3) an α of 0.5 and 1.2 was used. α of 0.98 and 1.1 matched the smFRET histograms for GTP-bound or GDP-bound, respectively. Note that the photon counting statistics in the experimental FRET system is sensitive to the timescale of moving between the open and closed states. If the conformational motion time is comparable to the time a single molecule dwells in the laser point ($\sim$1 ms), the FRET distribution will become unimodal. Since separated peaks were observed in the experimental data, the dynamics observed must have been slower than 1 ms. Nonetheless, since averaging always tends to compress the peaks, the simulation data, which was not averaged, was expected to have wider separation between the peaks. This was indeed observed (Figure S3C). Also, note that the sparsely-populated open state was indistinguishable from noise in the experimental GDP-bound histogram (Figure S3D). Thus, the open state population may be significantly smaller than $\alpha = 1.1$ produced. In this case, the free energy of GDP-bound open states would have been higher, leading to a larger contracting force $dG/d\ell$.

To ensure the sampling of rare states, particularly important for extended conformations of the GDP-bound dimer, umbrella sampling was used. The umbrella coordinate was the number of unique closed native contacts made between the BSE and G domain and, thus, ensured sampling from fully open to fully closed. The dimer simulations had two independent umbrella coordinates, one for each monomer. Unbiased histograms were obtained using the weighted histogram analysis method [60], and were used to calculate free energies.

The flexibility of hinge 1 (Figures 4B and S4) was estimated by a C_α SBM simulation equivalent to that just described except single basin, meaning that any term in the energy function containing the open structure was removed and $\alpha = 1$. Chain A of the apo (closed) crystal structure [10] was used to build the SBM. The PH domain along with stalk domain residues further than two nanometers from hinge 1 were frozen during the simulation, mimicking its filament-bound state. The temperature was the same as above (T=0.92) and the simulation was run for 10^8 time steps. For analysis of the structural fluctuations in terms of the helical coordinates, the frozen part of the stalk was fit to a stalk domain in the helical reconstruction of Figure 1C. Hinge 1 was identified by PRO322 and hinge 2 was identified by PRO27.

Stall force calculation

The mean force under the stall condition was determined by numerically integrating Eq. 1 using $P(\ell) = A\exp[G_{\rm GTP}(\ell)/{\rm k_B T}]$ and $F(\ell) = -dG_{\rm GDP}/d\ell$ obtained from molecular simulations, where A is a normalization constant for the probability distribution $P(\ell)$. In Eq. 1, we have $\sin\alpha = \Delta s/\ell$ with $\Delta s = \sqrt{\ell^2 - h^2}$; the positive sign in this equation means that only the links with $\Delta s > 0$ may be formed; the minimal possible length of a link is $\ell_{min} = h$. Functions $P(\ell)$ and $F(\ell)$ were discretized in 0.5 nm steps and it was assumed that the radius remains the same

in the two rungs.

An approximate analytical expression for the mean force can be obtained by assuming a flat probability distribution $P = 1/(l_{\max} - h)$ and constant force $F = F_0$. These choices are good approximations to the simulated distributions. Introducing such expressions for P and F into Eq. 1 gives

$$\langle F_s \rangle = \frac{\omega F_0}{l_{\max} - h} \int_h^{\ell_{\max}} \sin\alpha(\ell) d\ell \tag{3}$$

or explicitly

$$\langle F_s \rangle = \frac{\omega F_0}{l_{\max} - h} \left[\sqrt{l_{\max}^2 - h^2} + h \arctan \frac{h}{\sqrt{l_{\max}^2 - h^2}} - \frac{\pi h}{2} \right]. \tag{4}$$

Similarly, the transverse force is given by

$$\langle F_t \rangle = \frac{\omega F_0}{l_{\max} - h} \int_h^{\ell_{\max}} \cos\alpha(\ell) d\ell = \frac{\omega h F_0}{l_{\max} - h} \ln\left(\frac{l_{\max}}{h}\right). \tag{5}$$

Dynamin motor constriction model

A detailed formulation and analysis of the model for a dynamin filament on a membrane tube were given in a previous publication [24]. The dynamin filament was represented as an elastic polymer with each bead corresponding to a dynamin dimer. Stiffness constants for various elastic deformations of the polymer (i.e., the stretch k, the normal curvature κ, the twist τ, and the geodesic curvature β) were obtained from molecular simulations of dynamin tetramers or short filaments. The geometries of the continuous elastic system and its discretization are shown in Figure S6C,D. The elastic energy of the filament was

$$E_{\mathrm{F}} = \sum_{i=1}^{N} d_0 \left[\beta \left(\frac{\kappa_i}{\kappa_i^2 + \tau_i^2} \frac{\partial \tau_i}{\partial s} - \frac{\tau_i}{\kappa_i^2 + \tau_i^2} \frac{\partial \kappa_i}{\partial s} \right)^2 + \alpha_\kappa (\kappa_i - \kappa_0)^2 + \alpha_\tau (\tau_i - \tau_0)^2 + k(|\vec{r}_i - \vec{r}_{i-1}| - d_0)^2 \right] + E^{\mathrm{repu}} \tag{6}$$

Note that $E^{\mathrm{repulsion}}$ prevented the local pitch, i.e. axial distance between nearest neighbor filaments, from going below 8 nm.

The membrane tube description was based on an axially symmetric continuous Helfrich elastic membrane with stiffness χ and under tension γ. It was discretized into 4 nm disks for numerical simulations. The elastic energy of the membrane was

$$E_{\mathrm{M}} = \pi d_{\mathrm{M}} \left[\sum_{j=1}^{M} \left(\frac{\chi}{R_j} + 2R_j\gamma \right) + \chi \sum_{j=3}^{M-2} R_j \left(\frac{d^2[R_j]}{dz^2} \right)^2 \right] \tag{7}$$

The coupling energy between the filament and membrane was

$$E_{\mathrm{int}} = \frac{d_{\mathrm{M}}}{2} \epsilon_{\mathrm{int}} \sum_{i=1}^{N} \left[r_i - a - \bar{R}(i) \right]^2 \tag{8}$$

The separation between the center of the filament and the center of the membrane bilayer was $a = 8.5$ nm, which was taken from cryo-EM structures. The inner lumen radius (ILR) was defined as the membrane radius minus 2 nm (radius of dynamin stalk minus 10.5 nm), which assumed a 4 nm wide bilayer. The time evolution equations locally conserve membrane

area and the time scale was defined by a single lipid diffusion coefficient of 1 $nm^2/\mu s$. The filament beads were in contact with a thermal bath at 310 K, while thermal fluctuations in the membrane came only through contact with the beads. The mobility of a filament bead bound to the membrane, 1 $nm^2/\mu s$, was chosen to approximate the diffusion coefficient of single lipids within a bilayer. The lipid flows within the membrane are controlled by the same time scale [24]. A membrane stiffness $\chi = 24\ k_B T$ and tension $\gamma = 0.03\ k_B T/nm^2$ was used. The elastic energy cost of constricting the filament/membrane system was found to be dominated by the membrane energy (Figure S6F). The time step of 10 ns in numerical simulations was limited by the membrane description.

In the current study, the effects of motor GTPase activity are additionally included into the previous model. This is done in two ways.

In the AF model, we assume that every MM applies a constant force to its neighboring filament. Each simulation bead corresponds to a dynamin dimer and, thus, it has two MMs, one pointing up and one pointing down (along the axial direction). Therefore, the bead applies forces both to the filament above and below it. Each force has two components: $F_s(h)$ in filament direction and $F_t(h)$ in the axial direction; their magnitudes are given by solid lines in Figure 4E. Here, h is the separation between the bead and the neighboring filament, defined by the distance between the bead and a line segment connecting the two nearest beads on the neighboring filament less 2 nm, because of the displacement of the MM attachment points (Figure S6A,B). The force acting on the filament is shared between the beads that form the line segment. Note that MM dimers and their cycles are not explicitly resolved in this variant of the model; interactions between the motors are also neglected.

The more accurate EF model includes cross-dimers formed by MM dimers and resolves the kinetics of GTPase cycles. Again, each simulation bead corresponds to a stalk dimer and, thus, has two MMs associated with it. A MM undergoes transitions between the five ligand states of the GTPase cycle: Apo and with GDP, GTP, GTP-D or GDP-D (Figure 3D). The three monomeric states interconvert with the determined nucleotide on/off rates displayed in Table 1. The bulk concentrations of GTP and GDP are assumed to be 300 μM and 30 μM , respectively. The Apo and GDP states cannot form cross-dimers. Binding of GTP by a MM alters the conformational state from dominantly closed to dominantly open with an approximate rate of 300 s^{-1} (Figure 3C). Since this opening rate is relatively fast, it is not explicitly represented in the model, and, thus, all MM in the GTP state are assumed to immediately relax to the equilibrium open/closed distribution.

A MM monomer in the GTP state can transit to the dimeric GTP-D state which represents a weak pre-hydrolysis dimeric state. The GTP state transits to a GTP-D state at rate $k_{on}[MM]_{eff}$, provided that a valid MM partner exists. A partner MM is valid if it is also in the GTP state and if the generated cross-dimer would satisfy the conditions $\ell < \ell_{max}$ and $\Delta s > 0$ where the latter condition takes into account the asymmetry of hinge 1. The geometry is explained in Figure S6A. Additionally, due to the excluded volume of the MM dimer, a valid cross-dimer cannot intersect any existing cross-dimers (see Figure S7A). The broad free energy basin for GTP-bound dimers implies flexibility (Figure 4D) and, thus, no forces are generated by a GTP-D dimer. The GTP-D dimer dissociates into two GTP MMs at rate k_{off}.

The transition from a pre-hydrolysis GTP-D dimer to the post-hydrolysis GDP-D dimer

takes place at rate k_{hyd}. Note that hydrolysis was assumed to occur simultaneously in both monomers since the state of a hybrid dimer was unclear. Some justification for the assumption is found in our kinetic model result that hydrolysis occurs equally fast for dimers containing either two GTP molecules or one GTP and one GDP molecule (SI Section S1.1). The GDP-D dimer generated a force $\vec{f}(\ell)$ that had magnitude

$$f = \begin{cases} \frac{dG_{\text{GDP}}(\ell)}{d\ell}, & \ell < \ell_{\text{max}} \\ \frac{dG_{\text{GDP}}(\ell)}{d\ell}|_{\ell=\ell_{\text{max}}} + \eta(\ell - \ell_{\text{max}}), & \text{else.} \end{cases} \tag{9}$$

and was directed along the vector connecting the two MM attachment points (Figure S6A). The parameter η was set to 3 $\text{k}_\text{B}\text{T}/\text{nm}^3$, so that the force grew steeply when $\ell > \ell_{\text{max}}$. The Helmholtz free energy $G_{\text{GDP}}(\ell)$ for the GDP-bound dimer is shown in Figure 4D.

In accordance with the ratchet property of hinge 1, an additional force is applied between the two stalk beads when a dimer becomes slanted to the left ($\Delta s < 0$):

$$f_{\text{hinge}} = \begin{cases} \eta(\Delta s), & \Delta s < 0 \\ 0, & \text{else.} \end{cases} \tag{10}$$

The force f_{hinge} is along the $\phi-$direction, strongly opposing a decrease of Δs beyond zero. We found that the results of the model were essentially independent of η for two reasons. First, when cross-dimers stay formed at $\Delta s < 0$, the component of the contraction force along s is reversed and, thus, cross-dimers will eventually impede their own sliding at sufficiently negative Δs, even in the absence of f_{hinge} (Eq. 10). Second, the presence of many simultaneous cross-dimers mostly prevented membrane expansion from extending cross-dimers beyond ℓ_{max}, so the extension penalty in Eq. 9 has little effect. Even though the exact value of η is not important in Eq. 10, note that $\eta > 0$ is implicitly assumed by the rachet effect, i.e. transitions to the GTP-D state were only allowed for $\Delta s > 0$.

The transition from a GTP-D state to the GDP-D state is irreversible due to hydrolysis. The GDP-D state can be left through dissociation into two MM monomers, each in the GDP state, at rate k_{diss}. When the strain dependence of this rate was taken into account in the EF model, this was done by choosing

$$k_{\text{diss}}(\Delta s) = \begin{cases} k_{\text{diss}}, & \Delta s > 0 \\ \infty, & \text{else.} \end{cases} \tag{11}$$

Thus, an oppositely strained dimer dissociates immediately. In the EF model without strain dependence, k_{diss} remains constant regardless of the displacement Δs.

A particular realization of a stochastic trajectory, i.e. of a motor switching between states in its GTPase cycle, is typically (e.g. [61]) integrated by the Gillespie algorithm, which is a less expensive algorithm for simulating coupled kinetic processes because the technique is not limited to a time step controlled by the fastest process. Here, since integrating the equations of motion for the membrane and beads is already comparatively expensive, explicit simulation of the GTPase cycle within each MM is preferable to the more complicated coupling of a Gillespie calculation to the molecular dynamics. Explicit simulation had the additional advantage that any rates dependent on the geometry of the filament, e.g. strain dependence or dimerization,

were always in sync. The weighting times of transitions obey an exponential distribution with a single rate parameter, i.e. the probability of a transition with rate k within time Δt is $1 - \exp(-k\Delta t) \approx k\Delta t$ for $k\Delta t \ll 1$. The transition times (inverse of transition rates) between states were all much longer than the integration time step δt of 10 nanoseconds. Therefore, the probability of a transition occurring during a single time step was taken to be $k\delta t$. The small time step was dictated by the membrane description which captured lipid flows. Note that, since the GTPase cycle operates on a much slower time scale, a membrane treatment that ignored flows could have been used, particularly for short filaments, without impacting the kinetic results. As a point of reference, a one second simulation, i.e. 10^8 time steps, for a 200 bead filament on a 600 nm long membrane tube required 5 hours on a single core of an Intel Xeon E5-2695 v3 2.30GHz CPU.

The nucleotide association/dissociation rates are given in Table 1. Some GTPase-cycle parameters could not be directly measured (Figure 3D). Unless otherwise noted, $k_{\text{on}}[\text{MM}]^{\text{eff}} = 3 \times 10^5$ s^{-1}, $k_{\text{hyd}} = 175$ s^{-1}, and $k_{\text{off}} = 10^5$ s^{-1}. The duty ratio parameter ω was varied between 0.37 and 0.94 by varying k_{diss} between 100 s^{-1}and 3.3 s^{-1}. The values of ω lower than 0.37 in Figure 5A were obtained by also varying $[\text{MM}]^{\text{eff}}$. See SI Section S1.3 for further discussion of the choice of the GTPase cycle kinetic parameters.

References

[1] Ferguson, S. M & De Camilli, P. (2012) Dynamin, a membrane-remodelling GTPase. *Nat. Rev. Mol. Cell Biol.* **13**, 75–88.

[2] Morlot, S & Roux, A. (2013) Mechanics of dynamin-mediated membrane fission. *Annual Review of Biophysics* **42**, 629–649.

[3] Daumke, O, Roux, A, & Haucke, V. (2014) BAR domain scaffolds in dynamin-mediated membrane fission. *Cell* **156**, 882–892.

[4] Ramachandran, R & Schmid, S. L. (2018) The dynamin superfamily. *Current biology : CB* **28**, R411–R416.

[5] Faelber, K, Gao, S, Held, M, Posor, Y, Haucke, V, Noé, F, & Daumke, O. (2013) Oligomerization of dynamin superfamily proteins in health and disease. *Progress in molecular biology and translational science* **117**, 411–443.

[6] Antonny, B, Burd, C, De Camilli, P, Chen, E, Daumke, O, Faelber, K, Ford, M, Frolov, V. A, Frost, A, Hinshaw, J. E, Kirchhausen, T, Kozlov, M. M, Lenz, M, Low, H. H, Mcmahon, H, Merrifield, C, Pollard, T. D, Robinson, P. J, Roux, A, & Schmid, S. (2016) Membrane fission by dynamin: what we know and what we need to know. *EMBO J.* **35**, 2270–2284.

[7] Zhang, P & Hinshaw, J. E. (2001) Three-dimensional reconstruction of dynamin in the constricted state. *Nat. Cell Biol.* **3**, 922–926.

[8] Sundborger, A. C, Fang, S, Heymann, J. A, Ray, P, Chappie, J. S, & Hinshaw, J. E. (2014) A Dynamin Mutant Defines a Superconstricted Prefission State. *Cell Rep.* **8**, 734–742.

[9] Mattila, J.-P, Shnyrova, A. V, Sundborger, A. C, Hortelano, E. R, Fuhrmans, M, Neumann, S, Müller, M, Hinshaw, J. E, Schmid, S. L, & Frolov, V. A. (2015) A hemi-fission intermediate links two mechanistically distinct stages of membrane fission. *Nature* **524**, 109–113.

[10] Faelber, K, Posor, Y, Gao, S, Held, M, Roske, Y, Schulze, D, Haucke, V, Noé, F, & Daumke, O. (2011) Crystal structure of nucleotide-free dynamin. *Nature* **477**, 556–560.

[11] Ford, M. G. J, Jenni, S, & Nunnari, J. (2011) The crystal structure of dynamin. *Nature* **477**, 561–566.

[12] Kong, L, Sochacki, K. A, Wang, H, Fang, S, Canagarajah, B, Kehr, A. D, Rice, W. J, Strub, M.-P, Taraska, J. W, & Hinshaw, J. E. (2018) Cryo-EM of the dynamin polymer assembled on lipid membrane. *Nature* pp. 1–17.

[13] Luo, L, Xue, J, Kwan, A, Gamsjaeger, R, Wielens, J, Von Kleist, L, Cubeddu, L, Guo, Z, Stow, J. L, Parker, M. W, Mackay, J. P, & Robinson, P. J. (2016) The Binding of Syndapin SH3 Domain to Dynamin Proline-rich Domain Involves Short and Long Distance Elements. *J. Biol. Chem.* **291**, 9411–9424.

[14] Chappie, J. S, Acharya, S, Leonard, M, Schmid, S. L, & Dyda, F. (2010) G domain dimerization controls dynamin's assembly-stimulated GTPase activity. *Nature* **465**, 435–440.

[15] Chappie, J. S, Mears, J. A, Fang, S, Leonard, M, Schmid, S. L, Milligan, R. A, Hinshaw, J. E, & Dyda, F. (2011) A pseudoatomic model of the dynamin polymer identifies a hydrolysis-dependent powerstroke. *Cell* **147**, 209–222.

[16] Morlot, S, Galli, V, Klein, M, Chiaruttini, N, Manzi, J, Humbert, F, Dinis, L, Lenz, M, Cappello, G, & Roux, A. (2012) Membrane shape at the edge of the dynamin helix sets location and duration of the fission reaction. *Cell* **151**, 619–629.

[17] Dar, S & Pucadyil, T. J. (2017) The pleckstrin-homology domain of dynamin is dispensable for membrane constriction and fission. *Mol. Biol. Cell* **28**, 152–160.

[18] Roux, A, Uyhazi, K, Frost, A, & De Camilli, P. (2006) GTP-dependent twisting of dynamin implicates constriction and tension in membrane fission. *Nature* **441**, 528–531.

[19] Srinivasan, S, Dharmarajan, V, Reed, D. K, Griffin, P. R, & Schmid, S. L. (2016) Identification and function of conformational dynamics in the multidomain GTPase dynamin. *EMBO J.*

[20] Anand, R, Eschenburg, S, & Reubold, T. F. (2016) Crystal structure of the GTPase domain and the bundle signalling element of dynamin in the GDP state. *Biochemical and Biophysical Research Communications* **469**, 76–80.

[21] Chen, Y.-J, Zhang, P, Egelman, E. H, & Hinshaw, J. E. (2004) The stalk region of dynamin drives the constriction of dynamin tubes. *Nat. Struct. Mol. Biol.* **11**, 574–575.

[22] Kozlov, M. M. (2001) Fission of biological membranes: interplay between dynamin and lipids. *Traffic* **2**, 51–65.

[23] McDargh, Z. A, Vázquez-Montejo, P, Guven, J, & Deserno, M. (2016) Constriction by Dynamin: Elasticity versus Adhesion. *Biophys. J.* **111**, 2470–2480.

[24] Noel, J. K, Noé, F, Daumke, O, & Mikhailov, A. S. (2019) Polymer-like Model to Study the Dynamics of Dynamin Filaments on Deformable Membrane Tubes. *Biophys. J.* **117**, 1870–1891.

[25] Kozlovsky, Y & Kozlov, M. M. (2003) Membrane fission: model for intermediate structures. *Biophys. J.* **85**, 85–96.

[26] Pannuzzo, M, McDargh, Z. A, & Deserno, M. (2018) The role of scaffold reshaping and disassembly in dynamin driven membrane fission. *eLife* **7**, 2270.

[27] Lenz, M, Prost, J, & Joanny, J.-F. (2008) Mechanochemical action of the dynamin protein. *Phys. Rev. E* **78**, 011911.

[28] Chappie, J. S, Acharya, S, Liu, Y.-W, Leonard, M, Pucadyil, T. J, & Schmid, S. L. (2009) An intramolecular signaling element that modulates dynamin function in vitro and in vivo. *Mol. Biol. Cell* **20**, 3561–3571.

[29] Traut, T. W. (1994) Physiological concentrations of purines and pyrimidines. *Molecular and cellular biochemistry* **140**, 1–22.

[30] Binns, D. D, Barylko, B, Grichine, N, Atkinson, M. A, Helms, M. K, Jameson, D. M, Eccleston, J. F, & Albanesi, J. P. (1999) Correlation between self-association modes and GTPase activation of dynamin. *Journal of protein chemistry* **18**, 277–290.

[31] Binns, D. D, Helms, M. K, Barylko, B, Davis, C. T, Jameson, D. M, Albanesi, J. P, & Eccleston, J. F. (2000) The mechanism of GTP hydrolysis by dynamin II: a transient kinetic study. *Biochemistry* **39**, 7188–7196.

[32] Mohanakrishnan, A, Tran, T. V. M, Kumar, M, Chen, H, Posner, B. A, & Schmid, S. L. (2017) A highly-sensitive high throughput assay for dynamin's basal GTPase activity. *PLoS ONE* **12**, e0185639.

[33] Sweeney, H. L & Houdusse, A. (2010) Structural and functional insights into the Myosin motor mechanism. *Annual Review of Biophysics* **39**, 539–557.

[34] Veigel, C, Schmitz, S, Wang, F, & Sellers, J. R. (2005) Load-dependent kinetics of myosin-V can explain its high processivity. *Nat. Cell Biol.* **7**, 861–869.

[35] Oguchi, Y, Mikhailenko, S. V, Ohki, T, Olivares, A. O, De La Cruz, E. M, & Ishiwata, S. (2008) Load-dependent ADP binding to myosins V and VI: implications for subunit coordination and function. *Proc. Nat. Acad. Sci. USA* **105**, 7714–7719.

[36] Iwaki, M, Iwane, A. H, Shimokawa, T, Cooke, R, & Yanagida, T. (2009) Brownian search-and-catch mechanism for myosin-VI steps. *Nat. Chem. Biol.* **5**, 403–405.

[37] Kaya, M, Tani, Y, Washio, T, Hisada, T, & Higuchi, H. (2017) Coordinated force generation of skeletal myosins in myofilaments through motor coupling. *Nat. Commun.* **8**, 16036–16013.

[38] Chen, Y, Zhang, L, Graf, L, Yu, B, Liu, Y, Kochs, G, Zhao, Y, & Gao, S. (2017) Conformational dynamics of dynamin-like MxA revealed by single-molecule FRET. *Nat. Commun.* **8**, 15744.

[39] Gao, S, von der Malsburg, A, Dick, A, Faelber, K, Schröder, G. F, Haller, O, Kochs, G, & Daumke, O. (2011) Structure of myxovirus resistance protein a reveals intra- and intermolecular domain interactions required for the antiviral function. *Immunity* **35**, 514–525.

[40] Jana, B & Onuchic, J. N. (2016) Strain Mediated Adaptation Is Key for Myosin Mechanochemistry: Discovering General Rules for Motor Activity. *PLOS Comput. Biol.* **12**, e1005035.

[41] Shnyrova, A. V, Bashkirov, P. V, Akimov, S. A, Pucadyil, T. J, Zimmerberg, J, Schmid, S. L, & Frolov, V. A. (2013) Geometric catalysis of membrane fission driven by flexible dynamin rings. *Science (New York, NY)* **339**, 1433–1436.

[42] Kadosh, A, Colom, A, Yellin, B, Roux, A, & Shemesh, T. (2019) The tilted helix model of dynamin oligomers. *Proc. Nat. Acad. Sci. USA* **116**, 12845–12850.

[43] Cocucci, E, Gaudin, R, & Kirchhausen, T. (2014) Dynamin recruitment and membrane scission at the neck of a clathrin-coated pit. *Mol. Biol. Cell* **25**, 3595–3609.

[44] Morlot, S, Lenz, M, Prost, J, Joanny, J.-F, & Roux, A. (2010) Deformation of dynamin helices damped by membrane friction. *Biophys. J.* **99**, 3580–3588.

[45] Takeda, T, Kozai, T, Yang, H, Ishikuro, D, Seyama, K, Kumagai, Y, Abe, T, Yamada, H, Uchihashi, T, Ando, T, & Takei, K. (2018) Dynamic clustering of dynamin-amphiphysin helices regulates membrane constriction and fission coupled with GTP hydrolysis. *eLife* **7**, 393.

[46] Watanabe, S & Boucrot, E. (2017) Fast and ultrafast endocytosis. *Current opinion in cell biology* **47**, 64–71.

[47] Kabsch, W. (2010) Integration, scaling, space-group assignment and post-refinement. *Acta Crystallogr., Sect. D: Biol. Crystallogr.* **66**, 133–144.

[48] McCoy, A. J, Grosse-Kunstleve, R. W, Adams, P. D, Winn, M. D, Storoni, L. C, & Read, R. J. (2007) Phaser crystallographic software. *J. Appl. Crystallogr.* **40**, 658–674.

[49] Adams, P. D, Afonine, P. V, Bunkóczi, G, Chen, V. B, Davis, I. W, Echols, N, Headd, J. J, Hung, L.-W, Kapral, G. J, Grosse-Kunstleve, R. W, McCoy, A. J, Moriarty, N. W, Oeffner, R, Read, R. J, Richardson, D. C, Richardson, J. S, Terwilliger, T. C, & Zwart, P. H. (2010) PHENIX: a comprehensive Python-based system for macromolecular structure solution. *Acta Crystallogr., Sect. D: Biol. Crystallogr.* **66**, 213–221.

[50] Emsley, P & Cowtan, K. (2004) Coot: model-building tools for molecular graphics. *Acta Crystallogr., Sect. D: Biol. Crystallogr.* **60**, 2126–2132.

[51] Schuler, B, Lipman, E. A, & Eaton, W. A. (2002) Probing the free-energy surface for protein folding with single-molecule fluorescence spectroscopy. *Nature* **419**, 743–747.

[52] Schuler, B & Hofmann, H. (2013) Single-molecule spectroscopy of protein folding dynamics–expanding scope and timescales. *Curr. Opin. Struct. Biol.* **23**, 36–47.

[53] Müller, B. K, Zaychikov, E, Bräuchle, C, & Lamb, D. C. (2005) Pulsed interleaved excitation. *Biophys. J.* **89**, 3508–3522.

[54] Whitford, P. C, Miyashita, O, Levy, Y, & Onuchic, J. N. (2007) Conformational transitions of adenylate kinase: Switching by cracking. *J. Mol. Biol.* **366**, 1661–1671.

[55] Noel, J. K, Schug, A, Verma, A, Wenzel, W, Garcia, A. E, & Onuchic, J. N. (2012) Mirror images as naturally competing conformations in protein folding. *J. Phys. Chem. B* **116**, 6880–6888.

[56] Noel, J. K, Whitford, P. C, & Onuchic, J. N. (2012) The Shadow Map: A General Contact Definition for Capturing the Dynamics of Biomolecular Folding and Function. *J. Phys. Chem. B* **116**, 8692–8702.

[57] Pronk, S, Páll, S, Schulz, R, Larsson, P, Bjelkmar, P, Apostolov, R, Shirts, M. R, Smith, J. C, Kasson, P. M, van der Spoel, D, Hess, B, & Lindahl, E. (2013) GROMACS 4.5: a high-throughput and highly parallel open source molecular simulation toolkit. *Bioinformatics* **29**, 845–854.

[58] Noel, J. K, Levi, M, Raghunathan, M, Lammert, H, Hayes, R. L, Onuchic, J. N, & Whitford, P. C. (2016) SMOG 2: A Versatile Software Package for Generating Structure-Based Models. *PLOS Comput. Biol.* **12**, e1004794.

[59] Lammert, H, Schug, A, & Onuchic, J. N. (2009) Robustness and generalization of structure-based models for protein folding and function. *Proteins: Struct., Funct., Bioinf.* **77**, 881–891.

[60] Kumar, S, Rosenberg, J, Bouzida, D, & Swendsen. (1992) The weighted histogram analysis method for free-energy calculations on biomolecules. I. The method. *J. Comput. Chem.* **13**, 1011.

[61] Kubo, S, Shima, T, & Takada, S. (2020) How Cytoplasmic Dynein Couples ATP Hydrolysis Cycle to Diverse Stepping Motions: Kinetic Modeling. *Biophys. J.* **118**, 1930–1945.